ECS The Electrochemical Society
Advancing solid state & electrochemical science & technology

Investigating the Role of Mo and Cr during the Activation and Passivation of Ni-Based Alloys in Acidic Chloride Solution

View the article online for updates and enhancements.

ECS The Electrochemical Society
Advancing solid state & electrochemical science & technology

242nd ECS Meeting

Oct 9 – 13, 2022 • Atlanta, GA, US

Submit your abstract

Abstract submission deadline: **April 8, 2022**

Connect. Engage. Champion. Empower. Accelerate.

MOVE SCIENCE FORWARD

CrossMark

Investigating the Role of Mo and Cr during the Activation and Passivation of Ni-Based Alloys in Acidic Chloride Solution

Jeffrey D. Henderson,[1,=,*] Xuejie Li,[2,=] Fraser P. Filice,[1] Dmitrij Zagidulin,[1,**] Mark C. Biesinger,[1,3] Brad Kobe,[3] David W. Shoesmith,[1,3,***] Kevin Ogle,[2,**,z] and James J. Noël[1,3,**,z]

[1]*Department of Chemistry, Western University, London, ON N6A 5B7, Canada*
[2]*Chimie-ParisTech, PSL University, IRCP-CNRS, 75005 Paris, France*
[3]*Surface Science Western, Western University, London, ON N6G 0J3, Canada*

The elemental dissolution behaviour of commercially available Ni-based alloys was investigated in the context of surface activation, spontaneous passivation, and electrochemically-assisted passivation in hydrochloric acid solution using atomic emission spectroelectrochemistry (AESEC). Following surface activation, the spontaneous passivation of each alloy was found to proceed by the accumulation of mainly Mo-rich, but also Cr-rich oxides. An alloy's ability to recover from surface activation was found to improve with increased Mo content. For the alloy with the lowest Mo content considered here, approximately 8 wt.% Mo, spontaneous passivation was unsuccessful and active dissolution was observed. For alloys with higher Mo contents, greater than 13 wt.% Mo, spontaneous passivation occurred quickly, and dissolution rates stabilized at values comparable to those found for the native oxide, i.e., before perturbation by an applied potential. Mo(IV) oxides were found to be the species accumulating during spontaneous passivation using ex situ X-ray photoelectron spectroscopy (XPS). During electrochemically-assisted passivation, i.e., applying a potential within the passive region, a portion of the previously accumulated Mo was removed while Cr oxides accumulated at the surface. However, based on the dissolution rates observed after electrochemically-assisted passivation, Cr-content did not dictate the barrier layer properties.

Ni-based alloys containing various alloying elements, including both Cr and Mo, have become important industrial materials due to their corrosion resistance in aggressive environments. Serving as the alloy matrix, Ni can accommodate high concentrations of alloying elements while maintaining a single-phase (fcc) structure.[1] Alloying additions of Cr promote the formation of a Cr-rich barrier oxide, which is primarily responsible for protecting the underlying metallic substrate.[2,3] Alloying additions of Mo into Cr-containing alloys have been shown to result in the accumulation of oxidized Mo species on the outside of the Cr-rich oxide.[4] By itself, the Cr-rich oxide provides excellent protection in oxidizing environments; however, the presence of Mo species becomes increasingly important at low pH and high chloride concentration.[5,6] These conditions are commonly associated with localized corrosion processes, including both pitting and crevice corrosion.[7–9] Resistance to localized corrosion is influenced by the Mo content, which increases both film stability and repassivation behaviour.[4,5,10]

Alloying additions Cr and Mo are recognised to act synergistically in improving corrosion resistance, but many mechanistic features remain unclear. The current understanding of how Mo additions impact the corrosion behaviour of Cr containing alloys has been summarized by Lutton Cwalina et al.[11] First-principles calculations by Samin et al. demonstrated that additions of Mo enhance the adsorption of oxygen on the surface of Ni-Cr alloys.[12] Using in situ transmission electron microscopy, Yu et al. showed that during early-stage gas-phase oxidation, Mo additions decrease the formation of voids in the oxide layer formed on Ni-Cr alloys.[13] Using scanning tunnelling microscopy, Maurice et al. observed nanoscale surface defects in passivated Fe-Cr alloys.[14] When Mo was added to the alloy, defects were found to generate a

nanostructured "plug", which appeared to act as a healing phenomenon for the defects. Based on the observations in these studies, the influence of Mo can be generally summarized in terms of two main outcomes: increased oxide stability and improved ability to repair oxide film damage.

Currently, limited information has been published regarding the in situ (or in operando) dissolution behaviour of Ni-based alloys. This hinders efforts to optimize alloy composition, which requires a thorough understanding of how composition affects corrosion performance in a range of exposure conditions. Atomic emission spectroelectrochemistry (AESEC), and other similar techniques, have proven valuable in studying the in situ dissolution behaviour of corroding systems, including both active and passive systems.[15–17] In our previous study, the AESEC technique was used to reveal a previously unreported dynamic behaviour of alloyed Mo during the transpassive film breakdown on Ni-Cr-Mo alloys in 1 M NaCl.[18] Here, the dissolution behaviour of three commercial Ni-based alloys was investigated during surface activation, spontaneous passivation, and electrochemically-assisted passivation in 1 M HCl. Results obtained by AESEC were then compared to ex situ surface analyses performed by X-ray photoelectron spectroscopy (XPS).

Experimental

Materials.—Materials used in this study were provided by Haynes International in the form of mill-annealed sheets. To conform to the dimensions of the electrochemical flow cell used for AESEC measurements, samples were machined to 25 mm × 10 mm. The thickness of individual samples varied depending on the thickness of the original as-received sheet. Nominal alloy compositions, as reported by Haynes International, have been summarized in Table I. Alloy compositions are included in Table II, determined according to ASTM E1019-18, ASTM E1097-12, and ASTM E1479-16 procedures. These more accurate compositions were used in the quantification of AESEC measurements and will be referenced throughout the text.

Before experiments, sample surfaces were prepared using wet silicon carbide (SiC) paper. Samples to be used in electrochemical

=These authors contributed equally to this work.
*Electrochemical Society Student Member.
**Electrochemical Society Member.
***Electrochemical Society Fellow.
zE-mail: kevin.ogle@chimieparistech.psl.eu; jjnoel@uwo.ca

Table I. As reported by Haynes International, the nominal composition of Hastelloy samples are summarized. Values are given in wt.% where M indicates the maximum concentration of an individual alloying element, while, Bal. indicates the alloying element making up the balance due to fluctuations in composition.

Alloy	Ni	Cr	Mo	Fe	W	Cu	Co	Mn	V	Al	Si	C
BC-1	Bal.	15	22	2^M	—	—	—	0.25	—	0.5^M	0.08^M	0.01^M
C-22	Bal.	22	13	3	3	0.5^M	2.5^M	0.5^M	0.35^M	—	0.08^M	0.01^M
G-35	Bal.	33.2	8.1	2^M	0.6^M	0.3^M	1^M	0.5^M	—	0.4^M	0.6^M	0.05^M

Table II. Summary of the empirically determined compositions for alloy BC-1, C-22, and G-35. Values are given in wt.%. Analysis carried out by Cambridge Materials Testing Limited according to ASTM E1019–18, ASTM E1097–12, and ASTM E1479-16.

Alloy	Ni	Cr	Mo	Fe	W	Cu	Co	Mn	V	Al	Si	C
BC-1	60.9	14.4	22.10	0.85	0.01	0.03	—	0.25	—	0.18	<0.01	0.011
C-22	57.6	20.7	12.97	3.74	2.80	0.06	—	0.27	—	0.28	<0.01	0.012
G-35	56.3	33.4	7.98	0.54	0.07	0.02	—	0.45	—	0.24	<0.01	<0.010

measurements were ground using P600, P800, P1000, and P1200 grit SiC paper. Samples intended for surface analyses were further ground using P2500 and P4000 SiC paper, followed by polishing with a 1-μm diamond suspension. After surface preparation, samples were rinsed with Type-1 water, followed by ethanol, and then dried in a stream of high purity N_2 or Ar gas.

Experimental solutions were prepared with reagent grade HCl and Type-1 water. Quantification of inductively coupled plasma atomic emission spectroscopy (ICP-AES) data involved the use of standard solutions. These standards were prepared using aliquots of metal standards (SCP Science) directly in the experimental electrolyte (1 M HCl).

Electrochemical methods.—Electrochemical experiments were carried out using either a Reference 600 (Gamry Instruments, Warminster, PA, USA) or a Solartron Analytical model 1287 (Solartron Analytical, Hampshire, UK) potentiostat. Experiments were conducted in a custom-built PTFE flow cell designed for AESEC measurements. A brief description of this flow cell is provided below, with an extensive description having been published elsewhere.[16,19,20] The exposed area of the working electrode (WE) was limited to 1 cm². The flow rate in the WE compartment was maintained at ~2.75 ml min⁻¹ using a peristaltic pump. The counter (CE) and reference electrodes (RE) were housed in a second compartment, separated from the flow cell by an ionically conductive membrane. A saturated Ag/AgCl electrode (–0.197 V vs SHE) and a Pt flag served as the RE and CE, respectively. All electrochemical measurements were repeated at least once.

The temperature during electrochemical measurements was maintained at 75 °C by pre-heating the electrolyte and directly heating the WE affixed to the flow cell. Electrolyte temperatures were maintained by placing the solution reservoir in either an isothermal bath or on a hot plate. The WE temperature was maintained by placing a heating element directly on the back of the metal sample, in contact with the surface opposite to the flow cell. Here, the heating element was either a hollowed Cu heating disk connected to an isothermal bath or an electric heating assembly containing thermistors connected to a digital temperature controller, allowing for closed-loop temperature regulation. Together, these controls maintained experimental temperatures of 75 ± 1 °C during all experiments. All experiments were performed in naturally aerated solutions, apart from those conducted within a glove box for surface analysis, discussed below.

Both dynamic- and static-polarization experiments were conducted using the described experimental setup. Dynamic polarization experiments were initiated at –0.4 V (vs Ag/AgCl) and scanned positively at a scan rate of 0.5 mV s⁻¹, until a final potential of 1.0 V (vs Ag/AgCl). Static polarization experiments involved several

potential steps. Initially, samples were exposed to the solution at open-circuit as temperatures stabilized, then they were subjected to an applied potential of –0.8 V (vs Ag/AgCl) for 60 s, followed by a 300 s period at open circuit to facilitate relaxation. Samples were then subjected to an applied potential of 0.6 V (vs Ag/AgCl) for 60 s before again being released to open circuit (300 s) to facilitate relaxation. These two steps, cathodic and anodic polarization followed by an open circuit potential (OCP) measurement, were repeated three to four times each. Potentials used for cathodic and anodic polarization (–0.8 V and 0.6 V, respectively) were selected based on polarization behaviour observed during dynamic measurements, as well as procedures used in previous publications.[21]

AESEC measurements and data treatment.—The AESEC setup has been described in detail previously.[16,20] Briefly, situated downstream of the electrochemical flow cell is an ICP-AES instrument (Ultima 2C spectrometer, Horiba Jobin-Yvon, France). Species released during electrochemical experiments were carried from the WE surface by the flow of fresh electrolyte and injected into the plasma of the spectrometer. The emission intensity at wavelengths specific to each element was measured and used to quantify the instantaneous elemental dissolution rates of the alloy components.

Solution exiting the flow cell was introduced to the ICP using a Burgener PEEK Mira Mist® Nebulizer (Horiba Jobin-Yvon, France). Species exposed to the plasma operating at 1 kW and 40.68 MHz, undergo atomization and excitation, with the subsequent relaxation processes generating emission lines characteristic of the atom of origin. Independent mono- and polychromator optics allow the simultaneous monitoring of several emission lines. Since Mo was the alloying element present in the lowest concentrations, it was detected using the monochromator to provide increased spectral resolution. For experiments involving low dissolution rates, emission intensities exhibited poor signal-to-noise ratios. When necessary, data were treated with a boxcar average (n = 5) as used and discussed previously.[22] Unless otherwise stated, data were not subjected to averaging.

For the elements studied, emission lines and their detection limits are summarized in Table III. Experimental detection limits ($C_{3\sigma}$) were calculated using Eq. 1, where σ_B is the standard deviation of the background signal and α is the sensitivity factor determined from the calibration standards.

$$C_{3\sigma} = 3\frac{\sigma_B}{\propto} \qquad [1]$$

Standard calibration was used to convert time-varying emission line intensities into instantaneous concentrations (C_M). Values of C_M were then converted into instantaneous dissolution rates (ν_M)

Table III. Experimental emission lines and limits of detection.

Element	Wavelength/nm	Detection Limit, $C_{3\sigma}$/ppb (wt.)
Ni	231.60	10.8 ± 0.3
Cr	267.72	4.8 ± 0.2
Mo	202.03	1.4 ± 0.1

according to Eq. 2, where f is the flow rate and A the surface area of the WE.

$$\nu_M = f\frac{C_M}{A} \qquad [2]$$

Congruent and incongruent dissolution behaviours were distinguished by comparing metal ion ratios in the electrolyte to those in the bulk material. This was done by normalizing individual dissolution rates against the bulk alloying element, Ni, according to Eq. 3, where X_M is the mass fraction of alloying element M. Values used for mass fractions were determined from the empirical data in Table II to ensure accuracy.

$$\nu'_M = (X_{Ni}/X_M)\nu_M \qquad [3]$$

Features of increased, decreased, and congruent dissolution were identified relative to the bulk composition by considering normalized dissolution rates. For instance, congruent dissolution was observed when ν'_M was approximately equal to ν_{Ni}, i.e., alloying element M was dissolving at a rate proportional to its bulk alloy composition. When ν'_M exceeded values of ν_{Ni}, alloying element M was being selectively removed from the alloy matrix in comparison to Ni; i.e., the dissolution rate of M was higher than expected based on its bulk alloy composition. On the other hand, when ν'_M was less than ν_{Ni}, alloying element M was accumulating on the surface of the alloy; i.e., its dissolution rate was less than expected based on its bulk alloy composition. The quantity of excess M, Θ_M, at time, t, was calculated using Eq. 4.

$$\Theta_M = \int_0^t ((X_M/X_{Ni})\nu_{Ni} - \nu_M)dt \qquad [4]$$

Instantaneous dissolution rates were also converted into elemental current densities (j_M), that represent the ion fluxes in electrical units, according to Eq. 5, where F is Faraday's constant, m is the molar mass of metal M and, n is the number of electrons transferred in the oxidation reaction of metal M.

$$j_M = \frac{\nu_M F n}{m} \qquad [5]$$

To directly compare the elemental current densities, j_M, to the electrical current density, j_e, a convolution procedure was carried out to correct for the residency time in the flow cell and through the intermediate capillaries. Details of this convolution have been published previously.[16] Comparison of the sum of all elemental currents (j_Σ) with the convoluted electrochemical current density ($j*_e$) provides the opportunity to separate anodic current contributions leading to dissolution, oxide growth, gas evolution, etc.

XPS measurements.—Samples prepared for surface analysis underwent the identical electrochemical treatment used when making ICP-AES measurements but inside a N_2-purged glove box with the atmospheric O_2 content maintained at ∼50 ppm to minimize further oxidation following the electrochemical experiment. Solutions used for electrochemical treatments within the glove box required deaeration to help control the atmospheric O_2 concentration. This was done by sparging the solution with Ar gas before its introduction to the glove box. Upon the completion of electrochemical treatments, samples were transferred and stored in an
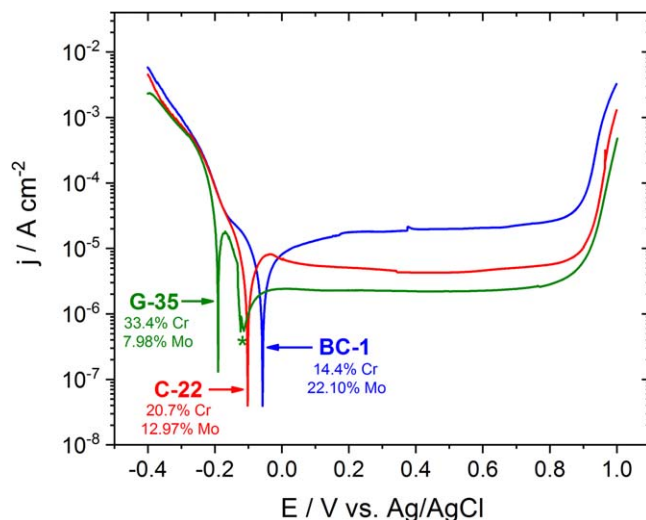

Figure 1. Polarization behaviour of alloys BC-1, C-22, and G-35 in 1 M HCl at 75 °C. For alloy G-35, the region of net cathodic current at applied potentials positive of the active-to-passive transition (–0.125 V to –0.113 V) is indicated (*). Alloy compositions (wt.%) shown here were taken from Table II.

Ar-purged glove box with an O_2 content maintained at <0.1 ppm to avoid oxidation during the period between preparation and XPS analysis. When required, samples were then introduced into the XPS instrument using a custom-built Ar-filled glove box connected directly to the spectrometer.

XPS measurements were carried out using a Kratos AXIS Supra spectrometer. All spectra were collected using a monochromatic Al Kα X-ray source (photon energy = 1486.6 eV) operating at 12 mA and 15 kV (180 W). During analysis, the pressure inside the analysis chamber was maintained at ⩽10⁻⁸ Torr. Calibration of the instrument work function was done using the binding energy (B.E.) of a standard metallic Au sample ($4f_{7/2}$ at 83.95 eV). In all spectra, photoelectrons were collected at a take-off angle of 90° from a 700 × 400 μm area. Survey spectra were recorded in a B.E. window from 0 to 1200 eV using a pass energy of 160 eV and a step size of 1 eV. High-resolution spectra of the C 1s, O 1s, Ni 2p, Cr 2p, Mo 3d, and S 2p lines were collected using a pass energy of 20 eV and a step size of 0.1 eV. All spectra were charge-corrected against the aliphatic (C–C) adventitious carbon signal set to 284.8 eV. All signal processing and deconvolution was performed with CasaXPS software (ver. 2.3.19) using a Shirley background subtraction. Deconvolution of high-resolution spectra was done using previously detailed fitting parameters and constraints collected from high-quality standard reference samples (Ni,[23,24] Cr,[23,25] Mo[26]).

Results and Discussion

Potentiodynamic polarization behaviour.—Current densities recorded during potentiodynamic scans on the three alloys in aerated 1 M HCl (75 °C) are presented in Fig. 1. Current densities associated with active dissolution were influenced by changes in Mo content, as shown previously,[5,6] with alloy G-35 (7.98 wt.% Mo) displaying the most pronounced active-to-passive transition and alloy BC-1 (22.10 wt.% Mo) showing no such transition. The values of zero-current potential ($E_{j=0}$) were also found to exhibit a positive shift as the Mo content was increased.

At more positive applied potentials all three alloys exhibited a potential-independent current density, indicating passivity until ∼0.85 V. At applied potentials ⩾0.85 V, the transpassive conversion of Cr(III) into soluble Cr(VI) species is observed.[27–29] As expected, alloys with larger Cr contents exhibited lower passive current densities, Fig. 1. At applied potentials positive of the active-to-passive transition for alloy G-35, the measured current density
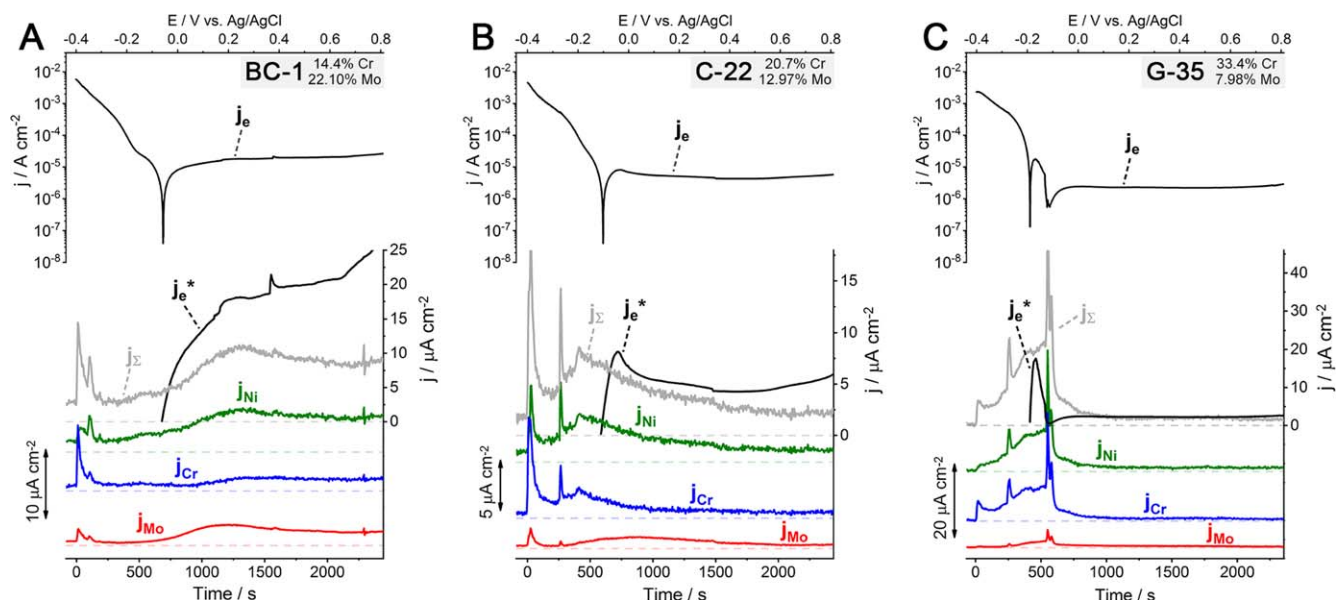
Figure 2. Comparison of the convoluted electrochemical current density (j_e*) with the instantaneous elemental (j_M) and sum current densities (j_Σ) for dynamic polarization experiments conducted in naturally aerated 1 M HCl at 75 °C. Both the untreated (j_e) and the convoluted (j_e*) electrochemical current densities are included for reference. The locations of $j = 0$ for j_Σ (and j_e*), j_{Ni}, j_{Cr}, and j_{Mo} are indicated by the dashed lines. Values of j_M were treated with a moving boxcar average ($n = 5$) in order to reduce noise resulting from relatively low dissolution rates. Alloy compositions (wt.%) shown here were taken from Table II.

switched from net anodic to net cathodic between ∼–0.13 and –0.11 V, as previously observed for this alloy and shown to be due to the reduction of O_2 dissolved in the solution.[30]

The electrochemical current densities (j_e) shown in Fig. 1, were compared to the elemental current densities obtained from AESEC measurements. The results obtained during the polarization of alloys (A) BC-1, (B) C-22, and (C) G-35, are shown in Fig. 2. To allow for the direct comparison of j_e with elemental current densities, j_M, where M was Ni, Cr, or Mo, a convolution procedure was carried out. This convolution procedure corrects j_e for the distribution of residence times through the flow cell and is detailed in a previous publication.[16] The comparison of the convoluted electrochemical current, j_e*, with the sum of all elemental current densities, j_Σ, provided information on the faradaic yield of the anodic reactions. In measurements presented here, species released from the alloy and detected by ICP-AES were assumed to have dissolved as Ni(II), Cr(III), and Mo(IV). Oxidation states were assigned based on both ex situ surface analyses, presented later in this study, and thermodynamic data.[31] For reference, the original (untreated) electrochemical current densities (j_e), plotted on log(j)-E axes, have been included at the top of Figs. 2a–2c while the values of j_e*, j_Σ, j_{Ni}, j_{Cr}, and j_{Mo}, are shown below, as a function of time.

For alloy BC-1, immediately following the application of –0.4 V (or $t = 0$), increases in j_{Ni}, j_{Cr}, and j_{Mo} were observed which quickly stabilized at low values within the cathodic region, Fig. 2a. At applied potentials $<E_{j=0}$, j_Σ stabilized at ∼5 μA cm^{-2}. As the applied potential was increased to values $>E_{j=0}$, j_Σ initially remained low, confirming the absence of an active region, before increasing to a maximum value of ∼10 μA cm^{-2}, which then persisted throughout the passive region. Comparing j_e* with j_Σ confirmed that a portion of the current measured by the potentiostat could not be accounted for by dissolution. In this case, differences between j_e* and j_Σ are the result of oxidation reactions unrelated to dissolution; i.e., the formation of oxidized surface species not detected by ICP-AES. This discrepancy, $j_\Sigma < j_e$*, which persisted through the passive region, can be attributed to film growth.[32] The difference between j_e* and j_Σ increased with increasing applied potential throughout the passive region suggesting that film growth was enhanced at higher potential, although obviously the effect of applied potential and exposure time cannot be entirely separated in potential sweep experiments.
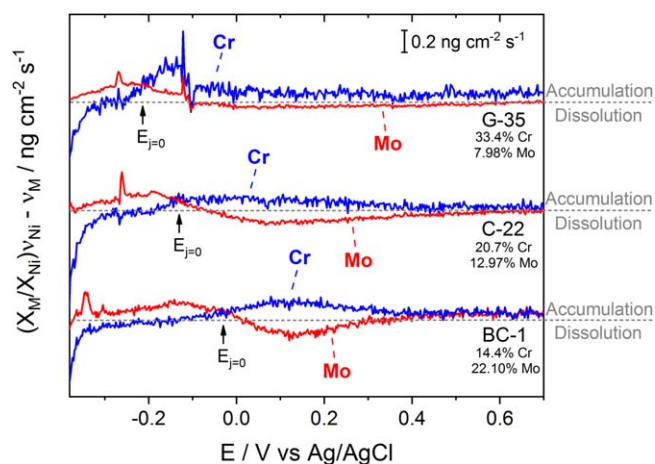

Figure 3. Trends in Cr and Mo accumulation and excess dissolution during dynamic polarization experiments, Fig. 1. Values of ν_{Ni} were normalized against the element M, either Cr or Mo. For each alloy, values of congruent dissolution ($y = 0$) are indicated by the dotted line. Alloy compositions (wt.%) shown here were taken from Table II.

Comparing the measurements made on alloy BC-1, Fig. 2a, to those made on alloys C-22 and G-35, Figs. 2b and 2c, revealed several similarities. Like on BC-1, the application of –0.4 V ($t = 0$) on alloys C-22 and G-35 resulted in momentary increases in j_{Ni}, j_{Cr} and j_{Mo}. Consistent with the role of Mo in suppressing active dissolution, the maximum value of j_Σ was lower for alloy C-22 (12.97 wt.% Mo) than for alloy G-35 (7.98 wt.% Mo). For alloy G-35, values of j_Σ exceeded values of j_e* during active dissolution, suggesting that some metal dissolution was coupled directly to cathodic reactions in this potential range, and therefore did not generate measurable net electrochemical current. At higher applied potentials, where film formation occurred, values of j_Σ were smaller than values of j_e* for both alloys, as also observed for alloy BC-1. This indicated an anodic contribution to film growth. Based on the difference between j_Σ and j_e*, film growth appeared highest for BC-1, followed by C-22, and lastly G-35. Nonetheless, the difference
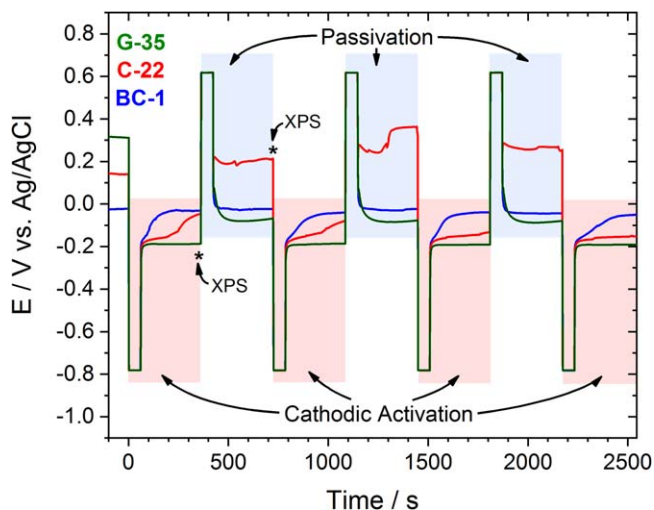
Figure 4. Measured potentials during potentiostatic experiments. Red-shaded areas indicate the surface activation process involving both cathodic activation (60 s at –0.8 V vs Ag/AgCl) and spontaneous passivation (300 s at open-circuit). Blue-shaded areas indicate the electrochemically-assisted passivation process involving the application of 0.6 V vs Ag/AgCl for 60 s, followed by a 300 s OCP measurement. Surface analysis by XPS was conducted at the indicated times (*).

between j_Σ and j_e* increased as the applied potential increased, although not as obviously for G-35.

The identity of the specific elements accumulating on the surface as oxides may be obtained by considering normalized dissolution rate information as a function of applied potential, Fig. 3. In this way, the potential regions of increased, decreased, and congruent dissolution were identified based on the bulk alloy composition. In the representation shown in Fig. 3, a positive value $((X_M/X_{Ni})\nu_{Ni} - \nu_M > 0)$ indicated that the dissolution rate of element M (either Cr or Mo) was less than expected based on its bulk composition in the alloy, indicating its accumulation at the surface. On the other hand, a negative value $((X_M/X_{Ni})\nu_{Ni} - \nu_M < 0)$ indicated that the dissolution rate of element M exceeded the value expected based on the alloy bulk composition; i.e., M was selectively removed from the surface. The separations between depletion (or excess dissolution) and accumulation are indicated along the right ordinate-axis, Fig. 3.

For all alloys, a transition between two distinct dissolution behaviours was found near the $E_{j=0}$. Below $E_{j=0}$, Cr was found to be the dominant cation released, while Mo species accumulated to some extent. However, at applied potentials higher than $E_{j=0}$, this trend was found to reverse, suggesting that a portion of the metal cations from the previously accumulated Mo species became the dominant species released and Cr species accumulated at the surface. While the data presented in Fig. 3 cannot quantify the amount of Mo species remaining in the surface film, ex situ surface analyses, discussed below with potentiostatic data, found that oxidized Mo species were present in relatively large quantities (12–32 at.%) for films formed at high applied potential. This is discussed in greater detail below. As the applied potential increased through the region where film formation occurred, i.e., at applied potentials higher than $E_{j=0}$, this opposing effect between accumulation of Cr species and dissolution of Mo species disappeared for BC-1 and C-22, indicating the formation of a film with a stable composition. This occurred at a lower potential for alloy BC-1 (22.10 wt.% Mo) than for alloy C-22 (12.97 wt.% Mo)—approximately 0.4 and 0.65 V, respectively. For the low Mo alloy G-35 (7.98 wt.% Mo), the accumulation of Cr species and dissolution of Mo species was maintained over the full potential range.

Although AESEC data collected during potentiodynamic polarization experiments highlighted changes in dissolution behaviour as a function of applied potential, the data were somewhat difficult to interpret. This was especially true in the context of film breakdown

and passivation behaviour, where both the applied potential and the time play an important role.[33] To further investigate the transition between the active and passive states, potentiostatic measurements were employed.

Potentiostatic polarization behaviour.—A potentiostatic approach was adopted, in which negative and positive applied potentials were used to force surface activation and passivation, respectively. Between the applied potentials, relaxation at open circuit was monitored. During both the applied potential and open circuit potential measurement period, dissolution behaviour was monitored with the premise being that the elemental dissolution rates are inversely proportional to the barrier properties of the film. Dissolution behaviour will be discussed in greater detail below. For all alloys, the potential measurements made during cyclic activation-passivation experiments are presented in Fig. 4, where cathodic activation and electrochemically-assisted passivation processes are indicated by the red- and blue-shaded regions, respectively. Furthermore, locations during the polarization cycle considered for subsequent surface analysis are indicated (*) in Fig. 4 and will be further discussed below.

Cathodic activation was initiated by applying a potential of –0.8 V, a polarization at which high cathodic current densities were observed, typically on the order of –10 mA cm^{-2}. During this period, H$_2$ evolution occurred at a high rate, experimentally observed as bubbles exiting the flow cell. Similar activation procedures have been employed previously.[21,29,34] The resulting surface activation was confirmed by increases in dissolution rate observed using ICP-AES. While the mechanism of this activation is not completely understood, it may be explained by either the removal or the degradation of the film by the introduction of defect sites in the oxide, by the partial reduction of the Cr(III) film to the more soluble Cr(II) species, and/or by the physical removal of oxide scale due to the rapid formation of gas bubbles at the surface. Previous studies have shown that applications of large negative potentials increase the number of defects in the oxide film,[35,36] thermodynamic calculations suggest the reduction of Cr(III) to Cr(II) at the applied potential used for cathodic activation,[21,31,37] and lastly, the possibility of releasing oxide scale from the surface cannot be omitted. The results presented here only demonstrate partial dissolution of excess Cr and Mo from the film and subsequent activation of the surface and do not allow for simple distinction between these mechanisms. Following surface activation and a period of open-circuit relaxation, electrochemically-assisted passivation occurred by the application of 0.6 V; this value was selected from the range of potentials where film formation was found to occur (see Fig. 1). Experimentally, cathodic activation and electrochemically-assisted passivation processes were cycled to investigate the effect of repeated surface activation.

Surface activation.—Potentials measured during the activation periods are indicated as red-shaded regions in Fig. 4. Before the first cathodic activation, i.e., t < 0 s, OCP values were related to the Cr-content of each alloy. Alloy G-35 (33.4 wt.% Cr) had the highest measured OCP, followed by C-22 (20.7 wt.% Cr), and lastly BC-1 (14.4 wt.% Cr). This was consistent with the influence of Cr-content on oxide films formed in relatively non-aggressive environments, in this case, an air formed (or native) oxide.[38] After being activated, i.e., after the polarization at –0.8 V, this trend was found to reverse. Once activated, the alloy's ability to re-establish an oxidized surface condition, as indicated by an increase in the OCP, was related to its Mo-content. In our previous work, we demonstrated that Mo-content was important to the stability of the oxide film, as well as in stifling active dissolution behaviour in acidic solutions.[39,40] It was shown that Mo accumulated on the surface under transpassive conditions was released to solution upon a return to passive conditions.[18] Above, we showed a similar accumulation/release mechanism applied for the transition from active to passive conditions, Fig. 3. Other studies have also highlighted the ability of alloyed Mo to improve corrosion resistance in acidic solutions.[6,41] In the data
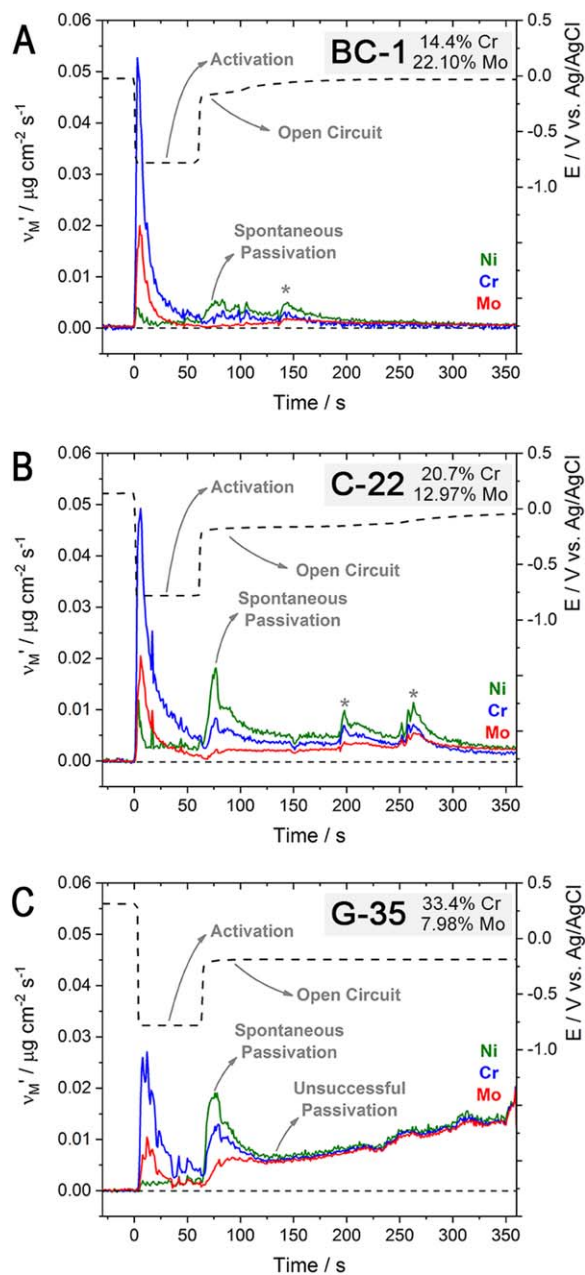
Figure 5. Normalized dissolution rates obtained during the first surface activation (–0.8 V vs Ag/AgCl) and subsequent open circuit potential measurement for alloy (a) BC-1, (b) C-22, and (c) G-35. All dissolution rates are normalized to the Ni-content in the alloy, Eq. 3. For clarity, dissolution transients observed during the spontaneous passivation process are indicated (*). The Cr and Mo contents (wt.%) shown here were taken from Table II.

presented here, alloys BC-1 (22.10 wt.% Mo) and C-22 (12.97 wt.% Mo) demonstrate increases in OCP after being activated, while the OCP of alloy G-35 (7.98 wt.% Mo) stabilized at relatively low values. For alloy BC-1, OCP values rapidly increased and stabilized at approximately –0.03 V, comparable to values measured before activation, i.e., $t < 0$ s. For alloy C-22, OCP values increased more slowly and stabilized at –0.05 V after the first activation, approximately 0.2 V below the OCP measured at $t < 0$ s. In the case of alloy G-35, OCP values stabilized quickly and did not increase with time. Instead, OCP values measured for alloy G-35 stabilized at –0.18 V, approximately 0.5 V below values measured at $t < 0$ s. While the behaviour of OCP remained consistent for repeated activation cycles, shown in Fig. 4, alloys BC-1 and C-22 both demonstrated

a weakened ability to recover with repeated active-passive cycles. In the case of alloy BC-1, achieving a steady-state condition during consecutive activation cycles required increasing amounts of time. In the case of alloy C-22, OCP values measured after activation periods were found to stabilize at lower values as the number of cycles increased.

The normalized dissolution rates, ν'_M, measured during the first cathodic activation process and the subsequent open circuit period are presented in Fig. 5. Since similar dissolution patterns were observed during repeated activation processes, only the first activation period will be discussed. However, the dissolution behaviour obtained for the full potentiostatic experiment (Fig. 4) has been included in the supporting information (Fig. S1 (available online at stacks.iop.org/JES/168/021509/mmedia)). Before the first cathodic activation, i.e., $t < 0$ s, the dissolved cation concentrations were below the limits of detection by ICP-AES, consistent with the presence of a protective oxide film. However, during the polarization at –0.8 V, a surge of metal dissolution was observed, confirming activation of the surface. During this activation process, labelled in Fig. 5, the values of both ν'_{Cr}, and ν'_{Mo} were found to be greater than that of ν_{Ni}, suggesting the excess dissolution of Cr and Mo from the electrode surface. For all alloys, Cr was found to be the dominant metal cation released from the surface, with smaller amounts of Mo also being released. This is consistent with the measured composition of oxides formed on Cr/Mo-containing alloys[32,42,43] and suggests the surface is activated by the partial removal of the oxide film during polarization at –0.8 V.

Upon release to open-circuit, again labelled in Fig. 5, alloys showed dissolution behaviour consistent with the spontaneous passivation of the surface. Both Cr and Mo species were found to accumulate at the surface (i.e., ν'_{Mo}, $\nu'_{Cr} < \nu_{Ni}$): however, the accumulation of Mo species dominated this process. This was consistent with observations made during dynamic-polarization experiments, where Mo species were found to be the dominant species accumulated at potentials below the apparent $E_{j=0}$ (see Fig. 3). Unsurprisingly, the ability of the surface to spontaneously passivate could be related to the Mo content of the alloy. Shown in Fig. 5a, alloy BC-1 (22.10 wt.% Mo) showed an immediate accumulation of Mo (and Cr) species, which quickly trended toward congruent dissolution (i.e., $\nu'_{Mo} = \nu'_{Cr} = \nu_{Ni}$) at a low overall dissolution rate. Comparison of the dissolution rates observed for the native oxide (i.e., $t < 0$ s) with those of the re-established passive oxide (i.e., $t > 250$ s), suggest the excellent ability of this alloy to recover from the surface activation process. This was consistent with the discussion of OCP values following activation, Fig. 4, which suggested that alloy BC-1 quickly returned to a state similar to that of the native oxide (i.e. $t < 0$ s). Values of OCP were approximately –0.02 V, regardless of whether the surface had been activated by cathodic polarization, electrochemically passivated (discussed below), or had a native oxide. The ability of alloy BC-1 to resist damage to the oxide film has been previously attributed to its high Mo content.[40,44]

As shown in the discussion of OCP, following the activation of alloy C-22, OCP values increased toward a plateau, Fig. 4, suggesting the re-establishment of an oxide layer. This was, however, significantly slower than the behaviour found for alloy BC-1, again suggested by the OCP. The dissolution behaviour shown in Fig. 5b, confirmed these observations, showing that alloy C-22 required a longer time than alloy BC-1 to spontaneously passivate and restore low dissolution rates following surface activation. Following the release to open-circuit, accumulation of both Cr and Mo species occurred, as observed for alloy BC-1. Elemental dissolution rates trended toward congruent behaviour and stabilized at low total dissolution rates, confirming the successful passivation of alloy C-22.

During the spontaneous passivation, momentary increases in elemental dissolution rates were occasionally observed for both alloy BC-1 and alloy C-22, indicated by (*) in Figs. 5a and 5b, although they were more frequent and severe for the lower-Mo-containing
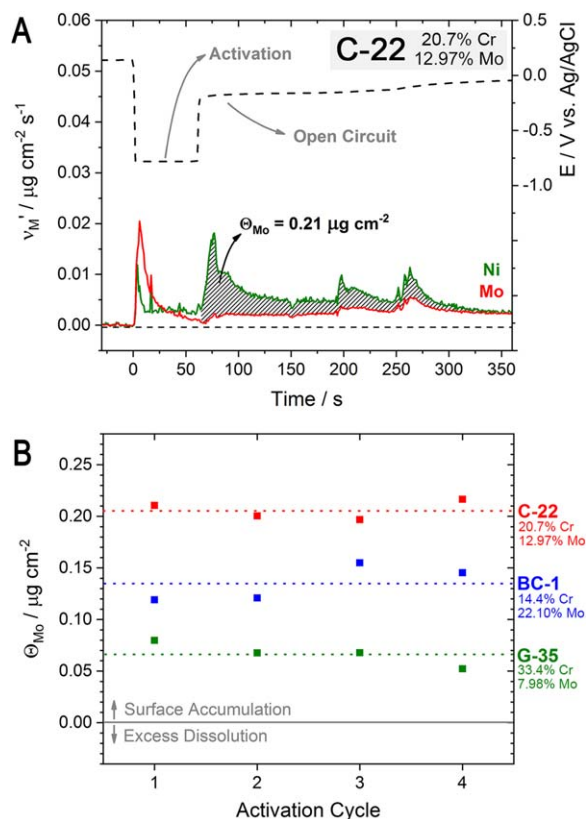
Figure 6. Quantification of Mo accumulation (Θ_{Mo}) during spontaneous passivation. (a) Graphical representation of the area considered as accumulation of Mo species during the first activation process on alloy C-22. (b) Values of Θ_{Mo} for repeated activation processes for all alloys. Dotted lines indicate calculated averages. The Cr and Mo contents (wt.%) shown here were taken from Table II.

alloy C-22. These dissolution transients are the result of film breakdown events during the early stages of passivation. Corresponding features were not observed during OCP measurements, when negative-going potential transients would be typical. When dissolution rates were converted into values of j_M and j_Σ, transients were found to correspond to current increases of between 9 and 31 $\mu A\,cm^{-2}$. An example of the converted currents can be found in the supporting information (Fig. S2). According to previously reported polarization resistance (R_P) values, these current transients are commonly accompanied by potential transients $\leqslant 3\,mV$.[30] During repeated activation processes, momentary increases in dissolution rates were consistently observed during the spontaneous passivation of alloy C-22 and, to a lesser extent for alloy BC-1. It is worth mentioning that with each dissolution transient, the separation between ν'_{Mo} (and ν'_{Cr}) and ν_{Ni} increased, suggesting an increased accumulation of Mo species following an "event" which then slowly approached congruent behaviour. When another event occurred, the separation (or accumulation) again increased, before approaching congruent behaviour. This behaviour is consistent with the role of alloyed Mo in the repair of localized breakdown events, which has been shown to occur by the deposition of Mo-rich species at sites of damage.[37,45]

As shown in Fig. 5c, the dissolution behaviour observed after the surface activation of alloy G-35 differed from that of BC-1 and C-22. While initially accumulation of Mo and Cr species was observed following the release to open circuit, after approximately 50 s the elemental dissolution became congruent and rates increased with time. Together the occurrence of congruent dissolution and the continuous increase in dissolution rates, may indicate unsuccessful passivation of alloy G-35. This is consistent with expectations for G-series alloys, which are not noted for their corrosion resistance to
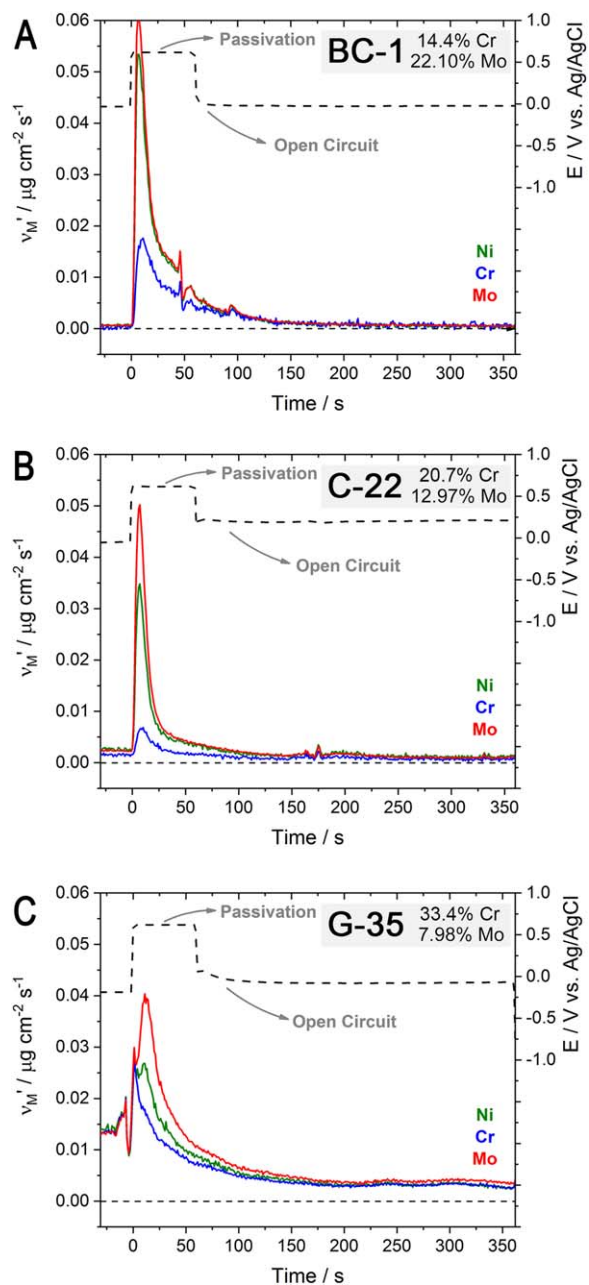

Figure 7. Normalized dissolution rates obtained during the first electrochemically-assisted passivation process (0.6 V vs Ag/AgCl) and subsequent open circuit potential measurement for alloy (a) BC-1, (b) C-22, and (c) G-35. All dissolution rates are normalized to the Ni-content in the alloy, Eq. 3. The Cr and Mo contents (wt.%) shown here were taken from Table II.

HCl solution as a result of their relatively low Mo contents, typically between 5 and 8 wt.%.[46,47] While alloy G-35 does contain a considerable amount of Mo, 7.98 wt.%, these differences in spontaneous passivation behaviour suggest some critical concentration of (or ratio between) alloyed Cr and Mo must exist to promote film stability in acidic Cl⁻-containing environments.

The extent of Mo species accumulation (Θ_{Mo}) was quantified during the spontaneous passivation processes using Eq. 4. A graphical representation of the area corresponding to accumulation of Mo species for alloy C-22 is highlighted in Fig. 6a as an example. The Θ_{Mo} values for all alloys obtained over repeated activation processes are shown in Fig. 6b. Although the accumulation of Mo species would be expected to scale with an alloy's Mo content, the experimentally determined values of Θ_{Mo} show that accumulation
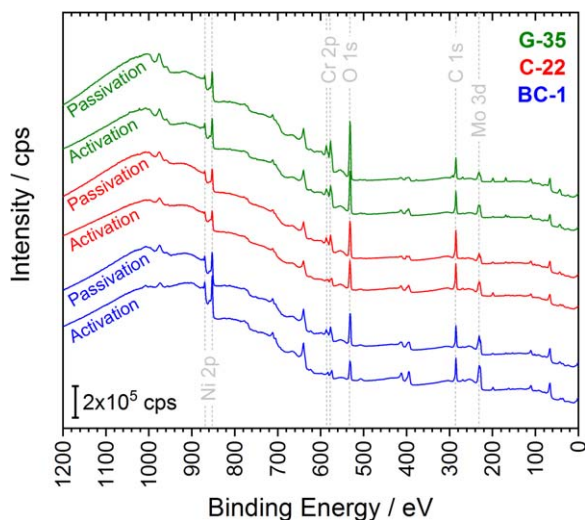
Figure 8. Comparison of survey spectra collected for alloys G-35, C-22, and BC-1 following activation and passivation processes. Experimental locations used to prepare samples for surface analysis are shown in Fig. 4. Quantification of the Ni2p$_{3/2}$, Cr 2p, Mo 3d, and O 1s peaks is given in Table IV.

Table IV. Surface composition (at.%) of G-35, C-22, and BC-1 after surface activation (including spontaneous passivation) and electrochemically-assisted passivation processes, considering the Ni2p$_{3/2}$, Cr 2p, and Mo 3d signals.

		Ni 2p$_{3/2}$	Cr 2p	Mo 3d
G-35	Activation	36.8	46.3	16.9
	Passivation	33.8	56.2	10.0
C-22	Activation	45.7	24.2	30.1
	Passivation	38.1	46.1	15.8
BC-1	Activation	52.5	14.8	32.7
	Passivation	42.4	32.3	25.3

increased according to: G-35 (7.98 wt.% Mo) < BC-1 (22.10 wt.% Mo) < C-22 (12.97 wt.% Mo). Furthermore, comparing values obtained over repeated activation cycles, alloy C-22 was found to consistently show the highest Θ_{Mo} value.

An explanation for this behaviour is based on the observations of the dissolution transients during the spontaneous passivation of alloy C-22 (Fig. 5b). There are two mechanisms by which Mo increases corrosion resistance that are largely agreed upon: however, their details remain an area of ongoing research.[11] First, Mo content is beneficial in establishing a stable oxide film, especially in acidic chloride media.[6] Here, during the spontaneous passivation process observed for alloys BC-1 and C-22, accumulation of Mo species was found to be dominant, as dissolution rates stabilized at low values. Second, Mo content is vital in the repair of localized breakdown events.[48] While BC-1 was able to quickly form a stable oxide film, and exhibited only small breakdown events, alloy C-22 displayed much larger breakdown events. During these events, the increased separation between ν'_{Mo} and ν_{Ni} indicated increased accumulation of Mo species following each event. Alloyed Mo is well known to promote the deposition of polymeric molybdate species at the breakdown site to stifle or block further dissolution.[37,45] If events are both frequent and severe, as for alloy C-22, one would expect the accumulation of Mo species at the surface to be greater than that at the surface of an alloy like BC-1 that experiences only minor breakdown events and more rapidly establishes a stable passivating oxide.

Electrochemically-assisted passivation.—Although the ability of the oxide film present on each alloy to recover from surface activation was of primary interest, the electrochemically-assisted passivation processes are also worth mentioning. Seen in the blue-shaded regions in Fig. 4, after the application of 0.6 V, OCP values were found to increase relative to the values measured after activation. This increase was most significant for alloy C-22, followed by G-35, and lastly BC-1. The normalized dissolution behaviour recorded during this process was similar for all alloys, Fig. 7. During the polarization at 0.6 V, all alloys showed the selective dissolution of Mo (i.e., $\nu'_{Mo} > \nu_{Ni}$) and the accumulation of Cr species ($\nu'_{Cr} < \nu_{Ni}$). While passive oxide films formed on Cr/Mo-containing alloys are known to accumulate both Cr and Mo species, the selective removal of Mo species observed here was believed to be the consequence of the previous surface activation and spontaneous passivation process. As discussed above, during spontaneous passivation all alloys were found to accumulate Mo species at their surfaces. Additionally, this was consistent with dynamic experiments (Fig. 3) which highlighted the excess dissolution of Mo and accumulation of Cr species at applied potentials higher than the apparent value of $E_{j=0}$. Previously, we demonstrated the dynamic nature of Mo species, which concentrate at the surface in the event of film breakdown and are partially released during the re-formation of Cr oxides.[18]

While the dissolution behaviour of all alloys suggested the re-formation of a Cr-rich surface film, differences in the electrochemically-assisted passivation behaviour were observed. In the case of alloys BC-1 and C-22, dissolution rates were found to quickly approach the limits of detection once the electrode potential was released to open-circuit. In contrast, alloy G-35 showed a significantly slower decrease in dissolution rates than the other alloys, despite having the highest Cr content (33.4 wt.% Cr), and established a steady-state congruent dissolution rate rather than re-establishing passivity. These differences suggest that a critical film composition is important in controlling the barrier layer properties in HCl solutions.

Surface analysis.—Surface compositions were determined after both surface activation (including spontaneous passivation) and electrochemically-assisted passivation using XPS. The experimental locations considered for surface analyses are indicated by (*) in Fig. 4. Since similar dissolution patterns were observed for repeated activation/passivation processes, the surface compositions were analyzed only following the first activation/passivation processes. Survey spectra obtained for the three alloys in both conditions are compared in Fig. 8. Subtle differences in the intensities of the Ni 2p, Cr 2p, and Mo 3d signals between the activated and passivated surface conditions were found. For all alloys, the intensity of the Mo 3d signal was higher following activation than it was for the passive surface condition. In contrast, the Cr 2p signal was higher following passivation than it was for the active surface condition. These changes, quantified using the Ni 2p$_{3/2}$, Cr 2p, and Mo 3d signals, are summarized in Table IV.

Since the oxidized alloy surface species were of primary interest here, the O 1s signal was not considered in the surface compositions listed in Table IV. Oxide films formed on various Cr-containing alloys during exposure to a variety of conditions are known to be on the order of a few nm thick.[15,42,49,50] Since the XPS has an effective analysis depth of 5–10 nm,[51] which is thicker than the oxide film, the photoelectron signals for Ni, Cr, and Mo obtained from survey spectra are expected to originate from both metallic and oxidized components. Information on oxide compositions was extracted by deconvolution of chemical state information present in high-resolution spectra.

High-resolution spectra obtained for the Ni 2p$_{3/2}$, Cr 2p$_{3/2}$, and Mo 3d photoelectron peaks, as well as the deconvoluted chemical states, for specimens analyzed after both activation and passivation are presented in Fig. 9. In all cases, the Ni 2p$_{3/2}$ signal was dominated by metallic Ni (86.4 to 100 at.%), as shown in Figs. 9a, 9d, and 9g. The

contributions from NiO and Ni(OH)$_2$ were found not to exceed a total of 13.6 at.%.

The high-resolution Cr 2p$_{3/2}$ spectra recorded on alloys BC-1 (Fig. 9b), C-22 (Fig. 9e), and G-35 (Fig. 9h), indicate mixtures of Cr$_2$O$_3$, Cr(OH)$_3$, and metallic Cr. This was true for both the activated and passivated surfaces. Following surface activation (and spontaneous passivation), the contribution from oxidized Cr species was relatively low compared to that of the metallic species, especially for the low-Cr alloy BC-1. The concentration of oxidized Cr species after activation was found to increase with increasing Cr content of the alloy, with BC-1 (14.4 wt.% Cr) < C-22 (20.7 wt.% Cr) < G-35 (33.4 wt.% Cr). The contributions from oxidized Cr species were higher following the electrochemically-assisted passivation process than those measured on alloys after surface activation (and spontaneous passivation).

Deconvolution of high-resolution Mo 3d spectra collected on the three alloys, BC-1 (Fig. 9c), C-22 (Fig. 9f), and G-35 (Fig. 9i), after both activation and electrochemically-assisted passivation processes, revealed a complex mixture of metallic and oxidized Mo species

(Mo(IV), Mo(V), and Mo(VI)). In some analyses, a small amount of S contamination was also observed. The S 2s signal, which overlapped with the Mo 3d signal, was subtracted using the chemical state information provided by analysis of the S 2p peak. The relative amount of oxidized Mo species was found to decrease on the electrochemically passivated surfaces compared to those which had been activated (and spontaneously passivated). This was consistent with AESEC results which demonstrated the tendency of Mo species to accumulate during spontaneous passivation and be removed during the electrochemically-assisted passivation process. The spectra in Fig. 9 indicate a clear preference for Mo(IV) surface species after spontaneous passivation, while Mo(VI) species dominated after electrochemically-assisted passivation. Thermodynamics supports the formation of higher valence state Mo species such as MoO$_3$ or MoO$_4$,[2–31] with the latter being known to undergo complex polymerization reactions at low pH.[37,45,52]

While deconvoluted high-resolution spectra provide information on the ratios of oxides to metal as well as the distribution of various oxidized species, they do not provide a true representation of what is
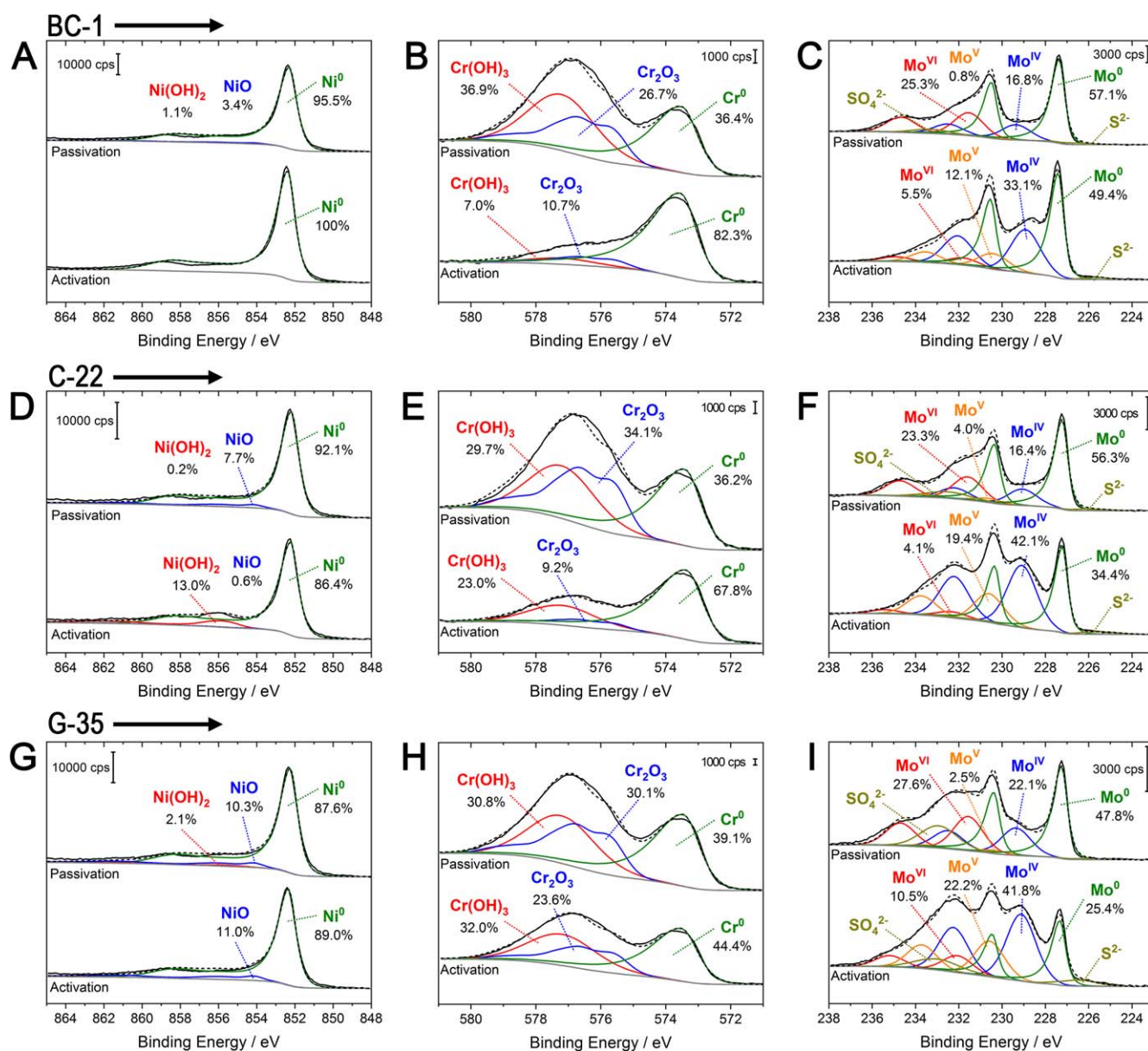

Figure 9. High resolution Ni 2p$_{3/2}$, Cr 2p$_{3/2}$, and Mo 3d spectra collected on alloys (a)–(c) BC-1, (d)–(f) C-22, and (g)–(i) G-35. Surface analysis was conducted after activation (bottom) and passivation (top) steps, as discussed for potentiostatic polarization data. Experimental data (solid black) are presented along with the resultant fits (dotted black curves) and individual components considered in the deconvolution (solid curves in various colours).
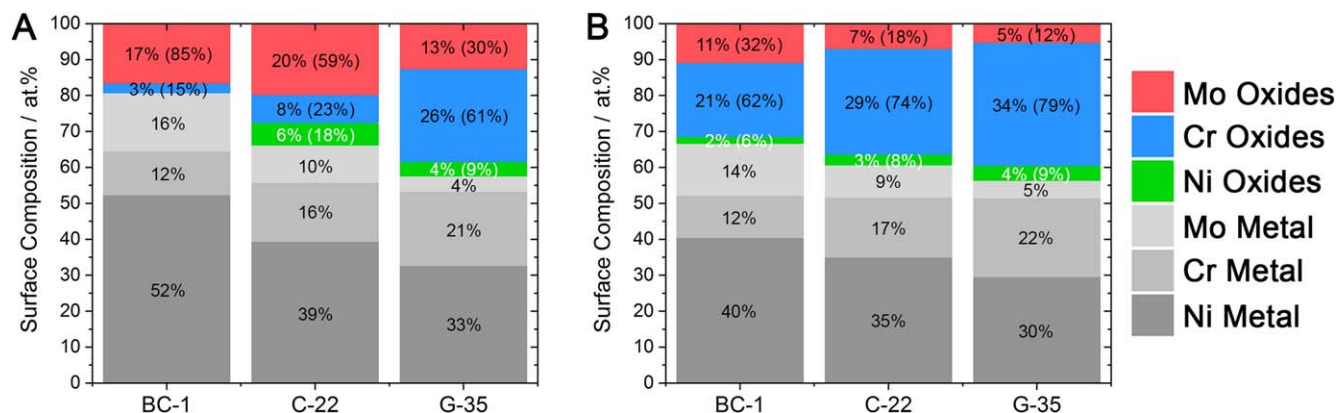
Figure 10. Surface compositions of BC-1, C-22, and G-35 after (a) surface activation and (b) electrochemically-assisted passivation processes. Experimental locations used to prepare samples for surface analysis are shown in Fig. 4. For the oxidized components, the relative oxide composition is also indicated in parentheses.

on the surface. A more representative analysis of surface composition can be obtained by coupling the information provided by the survey spectra (i.e., the average surface composition) and the deconvoluted high-resolution spectra (i.e., the relative speciation concentrations). Shown in Fig. 10, are the relative surface compositions expressed in terms of the metallic (Ni, Cr, and Mo) and oxidized contributions ($Ni(OH)_2$, NiO, Cr_2O_3, $Cr(OH)_3$, Mo(IV), Mo(V), and Mo(VI)).

After surface activation and spontaneous passivation, Fig. 10a, the amount of oxidized Mo surface species increased in the order G-35 < BC-1 < C-22, consistent with the trends observed by AESEC, as expressed by the values of Θ_{Mo}, Fig. 6b. Both the AESEC and XPS data indicate that alloy C-22 exhibits the largest amount of Mo-rich surface species following surface activation and spontaneous passivation. For surfaces analyzed after electrochemically-assisted passivation, Fig. 10b, all alloys demonstrated a decrease in oxidized Mo content and an increase in oxidized Cr content relative to their activated counterparts. This change was consistent with observations made by AESEC, which showed a tendency of Mo species to accumulate during spontaneous passivation (i.e., after activation) and subsequently be released alongside the accumulation of Cr-rich surface species during electrochemically-assisted passivation.

Conclusions

Using the operando measurements afforded by atomic emission spectroelectrochemistry (AESEC), the dissolution behaviour of Hastelloy BC-1, C-22, and G-35, was studied during the surface activation, spontaneous passivation, and electrochemically-assisted passivation in 1 M HCl (75 °C). Following surface activation, the accumulation of Mo species was found to dominate the spontaneous passivation behaviour, however, the accumulation of Cr species was also an important factor. After surface activation, high Mo content alloys, BC-1 (22.10 wt.% Mo) and C-22 (12.97 wt.% Mo), were found to rapidly recover, however, alloy C-22 required a slightly longer time and exhibited transient behaviour consistent with film breakdown. After processes of surface activation and spontaneous passivation, the accumulation of Mo species was found to be higher for alloy C-22 than for alloy BC-1, despite its lower Mo concentration. This was attributed to Mo deposition that occurred during the transient breakdown behaviour observed for alloy C-22 and not alloy BC-1. In the case of alloy G-35 (7.98 wt.% Mo), while an attempt to spontaneously passivate the activated surface was apparent, elemental dissolution rates rapidly increased, with congruent behaviour suggesting active dissolution. During electrochemically-assisted passivation processes, previously accumulated Mo species were found to be partially removed while accumulation of Cr species dominated the film formation process. The concept of Mo species accumulation and subsequent dissolution is consistent with previous

studies conducted on film breakdown/repair. Data acquired by AESEC were also compared to the results of ex situ XPS surface analysis. Both relative surface composition and oxidation state information were discussed, with connections made to the AESEC data. Most notably, the observation suggesting the large accumulation of Mo species on the moderate Mo content alloy (C-22) was consistent between both AESEC and XPS measurements. These findings suggest the dual role of alloy Mo in stabilizing and repairing the oxide film.

ORCID

Jeffrey D. Henderson https://orcid.org/0000-0001-7415-756X
Kevin Ogle https://orcid.org/0000-0002-1453-7082
James J. Noël https://orcid.org/0000-0003-3467-4778

References

1. J. R. Davis, *Nickel, Cobalt, and their Alloys* (ASM international, Materials Park, OH) (2000).
2. N. Priyantha, P. Jayaweera, D. D. Macdonald, and A. Sun, *J. Electroanal. Chem.*, **572**, 409 (2004).
3. X. Wu, S. Voyshnis, A. Seyeux, Y. Chumlyakov, and P. Marcus, *Corros. Sci.*, **141**, 175 (2018).
4. A. C. Lloyd, J. J. Noël, S. McIntyre, and D. W. Shoesmith, *Electrochim. Acta*, **49**, 3015 (2004).
5. N. S. Zadorozne, C. M. Giordano, M. A. Rodriguez, R. M. Carranza, and R. B. Rebak, *Electrochim. Acta*, **76**, 94 (2012).
6. A. Mishra, D. W. Shoesmith, and P. Manning, *Corrosion*, **73**, 68 (2017).
7. J. W. Oldfield and W. H. Sutton, *Br. Corros. J.*, **13**, 13 (1978).
8. J. W. Oldfield and W. H. Sutton, *Br. Corros. J.*, **13**, 104 (1978).
9. P. Marcus, *Corrosion Mechanisms in Theory and Practice* (CRC press, Boca Raton, FL) (2011).
10. K. Gusieva, L. K. Cwalina, W. H. Blades, G. Ramalingam, J. H. Perepezko, P. Reinke, and J. R. Scully, *J. Phys. Chem. C*, **122**, 19499 (2018).
11. K. Lutton Cwalina, C. R. Demarest, A. Y. Gerard, and J. R. Scully, *Current Opinions in Solid State & Materials Science*, **23**, 129 (2019).
12. A. J. Samin and C. D. Taylor, *Corros. Sci.*, **134**, 103 (2018).
13. X.-x. Yu, A. Gulec, C. M. Andolina, E. J. Zeitchick, K. Gusieva, J. C. Yang, J. R. Scully, J. H. Perepezko, and L. D. Marks, *Corrosion*, **74**, 939 (2018).
14. V. Maurice, H. Peng, L. H. Klein, A. Seyeux, S. Zanna, and P. Marcus, *Faraday Discuss.*, **180**, 151 (2015).
15. K. Lutton, K. Gusieva, N. Ott, N. Birbilis, and J. R. Scully, *Electrochem. Commun.*, **80**, 44 (2017).

16. K. Ogle and S. Weber, *J. Electrochem. Soc.*, **147**, 1770 (2000).
17. K. Ogle, J. Baeyens, J. Swiatowska, and P. Volovitch, *Electrochim. Acta*, **54**, 5163 (2009).
18. J. D. Henderson, X. Li, D. W. Shoesmith, J. J. Noël, and K. Ogle, *Corros. Sci.*, **147**, 32 (2019).
19. V. Shkirskiy, P. Maciel, J. Deconinck, and K. Ogle, *J. Electrochem. Soc.*, **163**, C37 (2016).
20. K. Ogle, *Corrosion*, **75**, 1398 (2019).
21. X. Li and K. Ogle, *J. Electrochem. Soc.*, **166**, C3179 (2019).
22. V. Shkirskiy, P. Keil, H. Hintze-Bruening, F. Leroux, P. Volovitch, and K. Ogle, *Electrochim. Acta*, **184**, 203 (2015).
23. M. C. Biesinger, B. P. Payne, A. P. Grosvenor, L. W. M. Lau, A. R. Gerson, and R. S. C. Smart, *Appl. Surf. Sci.*, **257**, 2717 (2011).
24. M. C. Biesinger, B. P. Payne, L. W. M. Lau, A. Gerson, and R. S. C. Smart, *Surf. Interface Anal.*, **41**, 324 (2009).
25. M. C. Biesinger, C. Brown, J. R. Mycroft, R. D. Davidson, and N. S. McIntyre, *Surf. Interface Anal.*, **36**, 1550 (2004).
26. P. A. Spevack and N. S. McIntyre, *J. Phys. Chem.*, **96**, 9029 (1992).
27. N. S. Zadorozne, C. M. Giordano, R. B. Rebak, A. E. Ares, and R. M. Carranza, *Procedia Materials Science*, **8**, 510 (2015).
28. D. D. Macdonald, A. Sun, N. Priyantha, and P. Jayaweera, *J. Electroanal. Chem.*, **572**, 421 (2004).
29. B. Laurent, N. Gruet, B. Gwinner, F. Miserque, K. Rousseau, and K. Ogle, *J. Electrochem. Soc.*, **164**, C892 (2017).
30. J. D. Henderson, B. Almusned, M. Momeni, S. Anderson, V. Dehnavi, D. Zagidulin, D. W. Shoesmith, and J. J. Noel, *J. Electrochem. Soc.*, **167**, 131512 (2020).
31. M. Pourbaix, *Atlas of Electrochemical Equilibria in Aqueous Solutions* (National Association of Corrosion Engineers, Houston, TX) 2nd English ed. (1974).
32. X. Zhang, D. Zagidulin, and D. W. Shoesmith, *Electrochim. Acta*, **89**, 814 (2013).
33. J. Velázquez, J. Van Der Weide, E. Hernández, and H. H. Hernández, *Int. J. Electrochem. Sci.*, **9**, 4129 (2014).
34. X. Li, J. Han, P. Lu, J. E. Saal, G. B. Olson, G. S. Frankel, J. R. Scully, and K. Ogle, *J. Electrochem. Soc.*, **167**, 061505 (2020).
35. P. Jakupi, D. Zagidulin, J. J. Noël, and D. W. Shoesmith, *Electrochim. Acta*, **56**, 6251 (2011).
36. X. Zhang, Z. Qin, D. Zagidulin, J. J. Noël, and D. W. Shoesmith, *J. Electrochem. Soc.*, **164**, C911 (2017).
37. X. Shan and J. H. Payer, *J. Electrochem. Soc.*, **156**, C313 (2009).
38. A. C. Lloyd, J. J. Noël, N. S. McIntyre, and D. W. Shoesmith, *J. Met.*, **57**, 31 (2005).
39. B. Kobe, M. Badley, J. D. Henderson, S. Anderson, M. C. Biesinger, and D. Shoesmith, *Surf. Interface Anal.*, **49**, 1345 (2017).
40. J. D. Henderson, N. Ebrahimi, V. Dehnavi, M. Guo, D. W. Shoesmith, and J. J. Noël, *Electrochim. Acta*, **283**, 1600 (2018).
41. M. B. Rockel, *Corrosion*, **29**, 393 (1973).
42. J. D. Henderson, A. Seyeux, S. Zanna, M. C. Biesinger, D. W. Shoesmith, J. J. Noël, and P. Marcus, *Corros. Sci.*, **159**, 108138 (2019).
43. L. Wang, A. Seyeux, and P. Marcus, *Corros. Sci.*, **165**, 108395 108395 (2020).
44. N. Ebrahimi, J. J. Noël, M. A. Rodriguez, and D. W. Shoesmith, *Corros. Sci.*, **105**, 58 (2016).
45. P. Jakupi, F. Wang, J. J. Noël, and D. W. Shoesmith, *Corros. Sci.*, **53**, 1670 (2011).
46. R. W. Revie, *Uhlig's Corrosion Handbook* (Wiley, New York) (2011).
47. U. Heubner, *Nickel Alloys* (CRC Press, Boca Raton, FL) (2000).
48. R. Newman, *Corros. Sci.*, **25**, 331 (1985).
49. E. Gardin, S. Zanna, A. Seyeux, A. Allion-Maurer, and P. Marcus, *Corros. Sci.*, **143**, 403 (2018).
50. T. Hanawa, S. Hiromoto, and K. Asami, *Appl. Surf. Sci.*, **183**, 68 (2001).
51. P. Van der Heide, *X-ray Photoelectron Spectroscopy: An Introduction to Principles and Practices* (Wiley, New York) (2011).
52. R. S. Lillard, M. P. Jurinski, and J. R. Scully, *Corros. Sci.*, **50**, 251 (1994).